Correspondence to:
P. O. Amaechi,
paoloobiaks@yahoo.fr

Ground-Based GNSS and C/NOFS Observations of Ionospheric Irregularities Over Africa: A Case Study of the 2013 St. Patrick's Day Geomagnetic Storm

P. O. Amaechi[1,2] , E. O. Oyeyemi[2] , A. O. Akala[2,3,4] , H. E. Messanga[5], S. K. Panda[6] , Gopi K. Seemala[7] , J. O. Oyedokun[2] , R. Fleury[8], and C. Amory-Mazaudier[9,10]

[1]Department of Physical Sciences, Chrisland University, Abeokuta, Nigeria, [2]Department of Physics, University of Lagos, Lagos, Nigeria, [3]Distance Learning Institute, University of Lagos, Lagos, Nigeria, [4]Institute of Maritime Studies, University of Lagos, Lagos, Nigeria, [5]Department of Geomatics, University of Yaounde, Yaounde, Cameroon, [6]Department of Electronics & Comm. Engineering, KL University, AP, India, [7]Indian Institute of Geomagnetism, Mumbai, India, [8]IMT Atlantique, Campus de Brest, France, [9]Sorbonne Universités, LPP, Polytechnique, Paris, France, [10]T/ICT4D, ICTP, Trieste, Italy

Abstract   In this paper, the variations of ionospheric irregularities have been studied using C/NOFS, ground-based GNSS and magnetometer measurements in Africa during the St. Patrick geomagnetic storm of March 17, 2013. The latitudinal distribution of irregularities was examined using GNSS-ROTI maps covering longitude 25°–45°E. Longitudinal characteristics were also investigated along with equatorial plasma bubbles (EPBs) and vertical drift velocity (Vz) from 12 to 21 March 2013. The results show postsunset irregularities from 12°S–27°N with the stronger ones confined within 1°S–7°S and 12°N–22°N in the prestorm period. The observed pre-reversal enhancement (PRE) with Vz varying from 22.51–59.47 m/s between 20.26 and 20.86 LT corresponded with the occurrence of EPBs. PRE greater than 40 m/s nevertheless, supported long lasting depletions. During the main phase, prompt penetration electric field enhanced the PRE thus, extended the latitudinal range of irregularities to 31°N. It also induced a long duration EPB along 15°E and several depletions over the Eastern sector. During the recovery phase, stormtime wind drove a conspicuous asymmetry in the morphology of the postsunset anomaly. This corresponded with the reduction in the latitudinal extent and strength of irregularities. Westward/eastward disturbance dynamo electric field inhibited/triggered irregularities in the postsunset/ postmidnight period on 18 March over the Eastern sector. The difference in the drift accounted for the longitudinal variations of irregularities before the storm. During the main phase however, irregularities were present (reduced) over the Eastern (Atlantic/Western) sectors. This difference might have been related to the changes in the wind inferred from the anomaly shape.

1. Introduction

Geomagnetic storms are temporary disturbances of the Earth's magnetosphere, hence its magnetic field. Their occurrences are usually associated with periods of intense and long lasting southward interplanetary magnetic field (IMF Bz) which interconnect with the geomagnetic field thereby, allowing for the transport of solar wind energy into the magnetosphere (Gonzalez et al., 1994, 1999). During geomagnetic storm, the electrodynamics of the ionosphere including electric field, current and neutral wind as well as key ionospheric parameters mainly the electron density, total electron content (TEC) and ionospheric irregularities undergo significant deviations from their quiet time behavior (Shreedevi & Choudhary, 2017; Woodman, 1970; L. Xu et al., 2008; Yue et al., 2016). These sudden and unpredicted changes can impact adversely the operational capability of critical Global Navigation Satellite System (GNSS) (Buonsanto, 1999) which have now found widespread usage in various endeavors including in the public, civil, military and industrial applications (de Abreu et al., 2017).

Ionospheric irregularities are small to large-scale structures in the plasma density (Perkins, 1975) which develop in the post sunset equatorial ionosphere through the non-linear evolution of the Rayleigh-Taylor (R-T) instability process (C. S. Huang & Hairston, 2015; Hudson & Kennel, 1975; Sultan, 1996; Woodman & La Hoz, 1976). They are often referred to as equatorial spread F (ESF) primarily because of their scattered and irregular signatures on ionograms (Berkner & Wells, 1934; Yizengaw & Groves, 2018). The optical

signature of the ESF is known as equatorial plasma bubbles (EPBs), corresponding to the irregular plasma density depletions captured by satellites and radars (Woodman & La Hoz, 1976) as well as GNSS- TEC (A. O. Akala et al., 2016).

The formation of EPBs can be significantly altered during geomagnetic storm mostly by the Prompt Penetration Electric Field (PPEF) (Nishida et al., 1966), the disturbance dynamo electric field (DDEF) (Blanc & Richmond, 1980) and trans-equatorial neutral wind (Maruyama & Matuura, 1984; Mendillo et al., 1992). For example, the regular pre-reversal enhancement (PRE) in the vertical $\mathbf{E} \times \mathbf{B}$ drift which is responsible for the uplift of the equatorial F-layer can be enhanced (reduced) by eastward (westward) PPEF (DDEF) in the postsunset period thereby, promoting the generation (inhibition) of EPBs (A. O. Akala et al., 2020; Amaechi et al, 2020a; Bhattacharyya et al., 2019; Dungey, 1956; B. J. Fejer et al., 1999; X. Luo et al., 2019; Tulasi Ram et al., 2006; Whalen, 2002).

The EPBs are sources of ionospheric scintillations which are mainly generated near the boundary of the bubbles where the plasma density is large (C. S. Huang, 2011). Scintillations manifest in the form of rapid fluctuations in the amplitude and/or phase of GNSS signals and can lead to loss of data, disruption of satellite links and reduction in the number of available satellites for navigation and positioning (Basu et al., 2005; Yizengaw & Groves, 2018). As such, understanding their variability especially, during transient space weather event such as geomagnetic storms is of utmost importance to the aeronomy community.

Of late, in situ measurements from Low Earth Orbit (LEO) satellites have proven crucial in understanding the dynamism of EPBs over least covered regions including Africa. For example, plasma density measurements have been obtained from the Republic of China Satellite (ROCSAT) (W. Luo et al., 2017; Su et al., 2006), the Communications/Navigation Outage Forecasting System (C/NOFS) (A. O. Akala et al., 2017; Yizengaw & Groves, 2018; Yizengaw et al., 2013; Zakharenkova et al., 2019) as well as the Defense Meteorological Satellite Program (DMSP) (Burke et al., 2004; C. Y. Huang et al., 2001) and Challenging Minisatellite Payload (CHAMP) (Stolle et al., 2006). These very important observations have revealed the prevalence of strong EPBs over Africa. The important findings from earlier studies emphasize the need for more irregularities studies over Africa with newer ground and space-based observations as multi-instrument studies were scanty over this region during past geomagnetic storms. Hence, further investigations with more datasets could at least assist in filling the global gap in knowledge caused by the long-time absence of ionospheric instruments over Africa and also help in complementing our understanding of the irregularities.

The St. Patrick's Day storms of 2013 and 2015 (17 March) were apparently intense events which occurred during the peak and descending phases of solar cycle24, respectively, albeit under relatively similar ionospheric profiles with different intensity, interplanetary and magnetic conditions (Sulungu & Uiso, 2019; Z. Xu et al., 2017). The storm of March 17, 2013 nevertheless, received lesser attention unlike that of March 2015. However, Shreedevi and Choudhary (2017) showed that the fluctuations in IMF Bz on March 17, 2013 led to westward electric field and a positive storm effect at the dip equator and in the entire low and mid-latitudes of the Indian sector instead of a negative storm. In the same vein, Yue et al. (2016) observed a positive storm effect during the initial and main phases of this storm. Results of their simulation using the Thermosphere Ionosphere Electrodynamics General Circulation Model (TIEGCM) revealed a long lasting negative storm over the Asian sector in addition to a hemispheric asymmetry driven by westward electric field and reduction in O/N_2. Dugassa et al. (2019) found that irregularities were stronger (weaker) over the American, (Western African) sector but absent over the Central and Eastern African as well as Indian longitude on March 17, 2013. However, they did not investigate the contribution of storm-time electric field in driving the observed differences especially over the African sector. Furthermore, there are virtually no works dealing with the latitudinal distribution of irregularities and their simultaneous variability in both hemispheres as well as their relation with changes in the post sunset anomaly in Africa during disturbed periods.

To this effect, we studied the characteristic of ionospheric irregularities using a combination of GNSS-TEC, ion density and drift measurements on board C/NOFS as well as magnetometer data over the low-latitude African region during the storm of March 17, 2013. We focused on features such as the (i) occurrence of EPBs and GNSS TEC irregularities in relation to the vertical plasma drift, (ii) latitudinal range of irregularities in line with changes in the post sunset EIA, and (iii) contribution of electric field in driving longitudinal
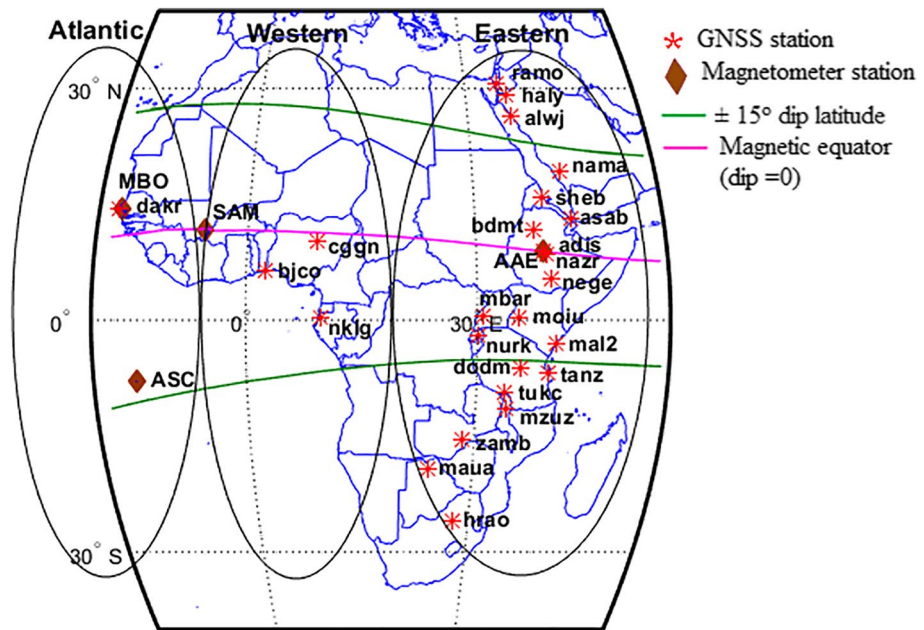
Figure 1. Geographic locations of GNSS and magnetometer stations. The red star (brown diamond) shows the GNSS (magnetometer) stations while the magenta (green) line indicates the location of the magnetic equator (±15° from the magnetic equator).

differences in irregularities. The striking similarities and differences of the African ionospheric responses to the March 17, 2013 and March 17, 2015 St. Patrick storms are also presented.

2. Data and Method

2.1. Data Sets

Interplanetary parameters in geocentric solar magnetospheric coordinates (GSM) recorded onboard the Advanced Composition Explorer (ACE) satellite were used to monitor solar wind conditions. These were: the x-component of the solar wind speed (Vx) and the z-component of the interplanetary magnetic field (IMF Bz). These data were time shifted by about 52 min to account for propagation delay (Amaechi et al., 2018a; Chakrabarty et al., 2005) and utilized to derive the y-component of the interplanetary electric field (IEFy).

Magnetic parameters were also obtained from the International Service of Geomagnetic Indices (ISGI). These were the Symmetric disturbance in the horizontal direction (SYM-H) and the Polar Cap (PC) indices. SYM-H was employed to monitor changes in the ring current (Iyemori & Rao, 1996) while PC was used as a quantitative estimate of joule heating (Troshichev et al., 2000).

Changes in the ionosphere during the magnetic perturbation were examined using GNSS- TEC provided by the UNAVCO Consortium. TEC data were used to reconstruct the Equatorial Ionization Anomaly (EIA) in the postsunset and compute the rate of TEC index (ROTI) which is a suitable proxy for ionospheric irregularities (Pi et al., 1997).

We equally utilized the Ion Velocity Meter (IVM) measurements of ion density (Ni) and meridional component of the ion drift velocity (Vz) provided by the C/NOFS CINDI payload. Both data sets were sampled at 1 Hz. The Ni profile was examined in order to detect eventual depletions herein referred to as EPBs. Vz on the other hand was employed as a proxy for the E × B vertical plasma drift. C/NOFS is a prototype operational system designed to monitor and forecast ionospheric irregularities in real-time and on a global scale. More information on it can be found in de La Beaujardière et al. (2004).

Finally, we obtained magnetometer measurements made available by Intermagnet for the stations in Addis Ababa (AAE), Mbour (MBO), and Ascension Island (ASC) as well as those of the station in Samogossoni

Table 1
Geographic Distribution of GNSS and Magnetometer Stations in the Eastern, Western, and Atlantic Longitudinal Sectors

Longitudinal sector	Station/Country	Station code	Geographic latitude	Geographic longitude	Magnetic latitude
		GPS station			
Eastern	Mitzpe Ramon	ramo	30.61°N	34.80°E	23.38°
	Halat Ammar, Saudi Arabia	haly	29.16°N	36.07°E	21.87°
	Al Wajh, Saudi Arabia	alwj	26.46°N	36.38°E	18.73°
	Nama, Saudi Arabia	nama	19.21°N	42.05°E	11.49°
	Sheb, Eritrea	sheb	15.85°N	39.05°E	7.36°
	Asab, Eritrea	asab	13.06°N	42.65°E	4.91°
	Bahir Dar, Ethiopia	bdmt	11.59°N	37.59°E	2.66°
	Nazret, Ethiopia	nazr	8.57°N	39.29°E	-0.25°
	Addis Ababa, Ethiopia	adis	9.03°N	38.77°E	0.16°
	Negele, Ethiopia	nege	5.33°N	39.59°E	-3.60°
	Eldoret, Kenya	moiu	0.29°N	35.29°E	-9.17°
	Mbarara, Uganda	mbar	0.60°N	30.74°E	−10.22°
	Kigali, Rwanda	nurk	1.94°S	30.09°E	−11.62°
	Malindi, Kenya	mal2	2.99°S	40.19°E	−12.42°
	Dodoma, Tanzania	dodm	6.17°S	35.75°E	−16.08°
	Tanzania CGPS, Tanzania	tanz	6.77°S	39.21°E	−16.59°
	Tukuyu, Tanzania	tukc	9.33°S	33.75°E	−19.59°
	Mzuzu, Malawi	mzuz	11.43°S	34.00°E	−21.88°
	Lusaka, Zambia	zamb	15.42°S	28.31°E	−26.26°
	Ngamiland, Botswana	maua	19.19°S	23.85°E	−30.11°
	Hartebeesthoek, South Africa	hrao	25.89°S	27.68°E	−36.32°
Western	Libreville, Gabon	nklg	0.35°N	9.67°E	−8.05°
	Cotonou, Benin	bjco	6.38°N	2.45°E	−3.08°
	Toro, Nigeria	cggn	10.12°N	9.12°E	0.78°
Atlantic	Dakar, Senegal	dakr	14.44°N	17.44°W	2.34°
		Magnetometer station			
Eastern	Addis Ababa, Ethiopia	AAE	9.03°N	38.77°E	0.16°
Western	Samogossoni, Mali	SAM	11.60°N	5.77°W	0.18°
Atlantic	Mbour, Senegal	MBO	14.39°N	16.96°W	2.06°
	Ascension Island	ASC	7.95°S	14.38°W	−12.34°

(SAM) which is provided by the West African Magnetometer Network (WAMNET). The magnetometer data were employed to compute the horizontal component of the Earth's magnetic field (H) and derive equatorial electric field proxy indices. The geographic location and coordinates of the GNSS and magnetometer stations are shown in Figure 1 and Table 1, respectively.

2.2. Data Processing

The quality of GNSS data was checked using the Translating Editing and Quality Checking software (Estey & Meertens, 1999). They were thereafter processed using the GPS-TEC program developed at Boston College (Seemala & Delay, 2010; Seemala & Valladares, 2011). The analysis procedure included the estimation of relative slant TEC (STEC) using the phase and code values for both L1 and L2 GPS frequencies (Sardón &

Zarraoa, 1997), the computation of absolute TEC by removal of satellites biases provided by the University of Bern as well as the receiver biases calculated by minimizing the TEC variability between 0200 and 0600 LT (Valladares et al., 2009), and the conversion of STEC to VTEC using the thin shell ionospheric model with Ionospheric Pierce Point (IPP) taken at 350 km. An elevation cut-off of 40° was considered in order to minimize multipath errors but also to reduce errors related to the changes in the ionospheric pierce point (IPP) caused by ionospheric gradient over the equatorial region (Rama Rao et al., 2006).

ROTI was computed as the standard deviation of the rate of change of TEC (ROT) in TECU/min every 5 min for each visible satellite over a ground station (Amaechi et al., 2018b; Cherniak et al., 2018; Maruyama et al., 2013; Pi et al., 1997). Daily ROTI maps were generated for longitude 25°–40°E with a latitudinal extent of 40°S–40°N by binning and averaging all ROTI values within 1 h and 1° latitude from 12 to 21 March 2013.

Vz is the component of the drift perpendicular to the magnetic field lines in the meridian plane. We restricted the data within $\pm$ 5° dip latitude where the magnetic field lines are quasi horizontal. This ensured that Vz presented accurately the $\mathbf{E} \times \mathbf{B}$ vertical plasma drift (C. S. Huang & Hairston, 2015). We additionally removed outliers from the time series data by applying a 15 point median filter and further smoothened them with a 9 point moving mean (Rodrigues et al., 2011). As such, only Vz and Ni data located close to the magnetic equator during the local postsunset to postmidnight period were considered. Consequently, the satellite's altitude was lesser than 500 km.

The ionospheric electric current disturbance (Diono) was computed using Equation 1. Diono is the magnetic disturbance due to ionospheric electric current (Le Huy & Amory-Mazaudier, 2005).

$$\text{Diono} = \text{H} - \text{SYM} - \text{H.cos}(\lambda) - \text{S}_\text{R} \tag{1}$$

where H is the observed component of the geomagnetic field, λ is the magnetic latitude of the station and S_R is the daily quiet regular variation of H due to the solar quiet (Sq) system. S_R was estimated by taken the average of 4 quiet days (*Kp* < 3) before the storm (Nava et al., 2016).

At low latitude, Diono is the sum the magnetic disturbance related to the disturbance polar no. 2 (DP2) fluctuations (Nishida, 1968) during PPEF and the magnetic disturbance related to the disturbance dynamo (Ddyn) (Le Huy & Amory-Mazaudier, 2005).

$$\text{Diono} = \text{DP2} + \text{Ddyn} \tag{2}$$

Both signals were extracted from Diono using appropriate filters. For the extraction of DP2 fluctuations which have periods lesser than 4 h were applied a high-pass filter. For the isolation of Ddyn signals with diurnal period, we utilized a band-pass filter with bandwidth of 8 h centered at 24 h (Nava et al., 2016).

## 3. Results

3.1. Interplanetary and Geomagnetic Conditions

Figure 2 shows variations of *Vx*, IMF Bz, IEFY, PCN, and PCS as well as SYM-H from 12 to 21 March 2013. 13 March was a relatively quiet day with *Kp* < 3. In addition, IMF Bz, IEFy, and PC indices were all stable and close to 0. This day was thus, considered as a reference quiet day. Generally, four periods of increase in PC indices were identified on 15–17 March and 20–21 March. These corresponded with epochs of southward IMF Bz and increased in eastward IEFy. The IMF Bz minima were: −9.55 nT (07:12 UT on 15 March); −5.60 nT (04:00 UT on 16 March); −19.06 and −9.81 nT (08:41 and 18:45 UT on 17 March). Other significant features in Figure 1 include the: (i) sudden impulse (SI) in SYM-H to 26 nT at 05:26 UT with related increase in Vx to 465 km/s on 15 March, (ii) sharp increase to 33 nT at 06:00 UT and corresponding Vx increase to 664 km/s on 17 March, (iii) two-step decrease in SYM-H (−107 nT at 10:28 UT and −132 nT at 20:52 UT). In addition, we noted an increase in Vx to 679 km/s on 20 March during the recovery phase and a decrease in SYM-H to −67 nT at 19:40 UT on 21 March with the equivalent changes in IMF Bz, IEFy and PC parameters.
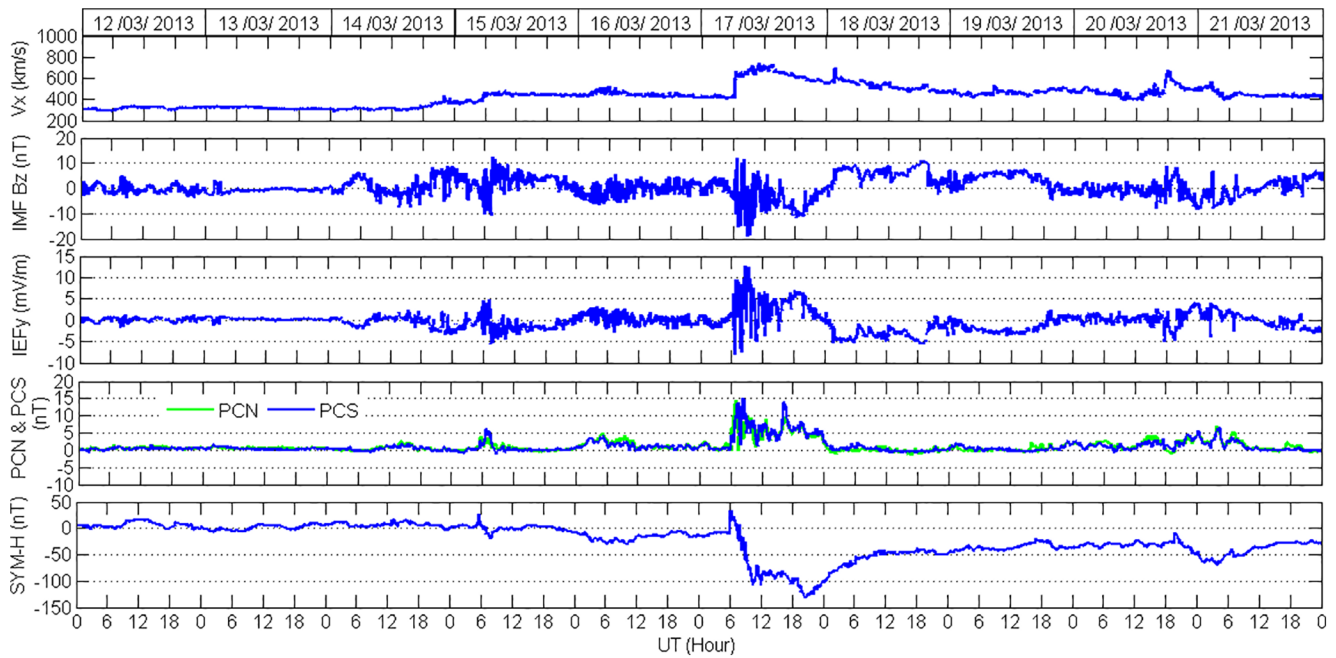
Figure 2. Variations of the solar wind speed (Vx), interplanetary magnetic field (IMF Bz), Interplanetary electric field (IEFY), Polar cap indices (PCN and PCS), and SYM-H index on 12–21 March 2013.
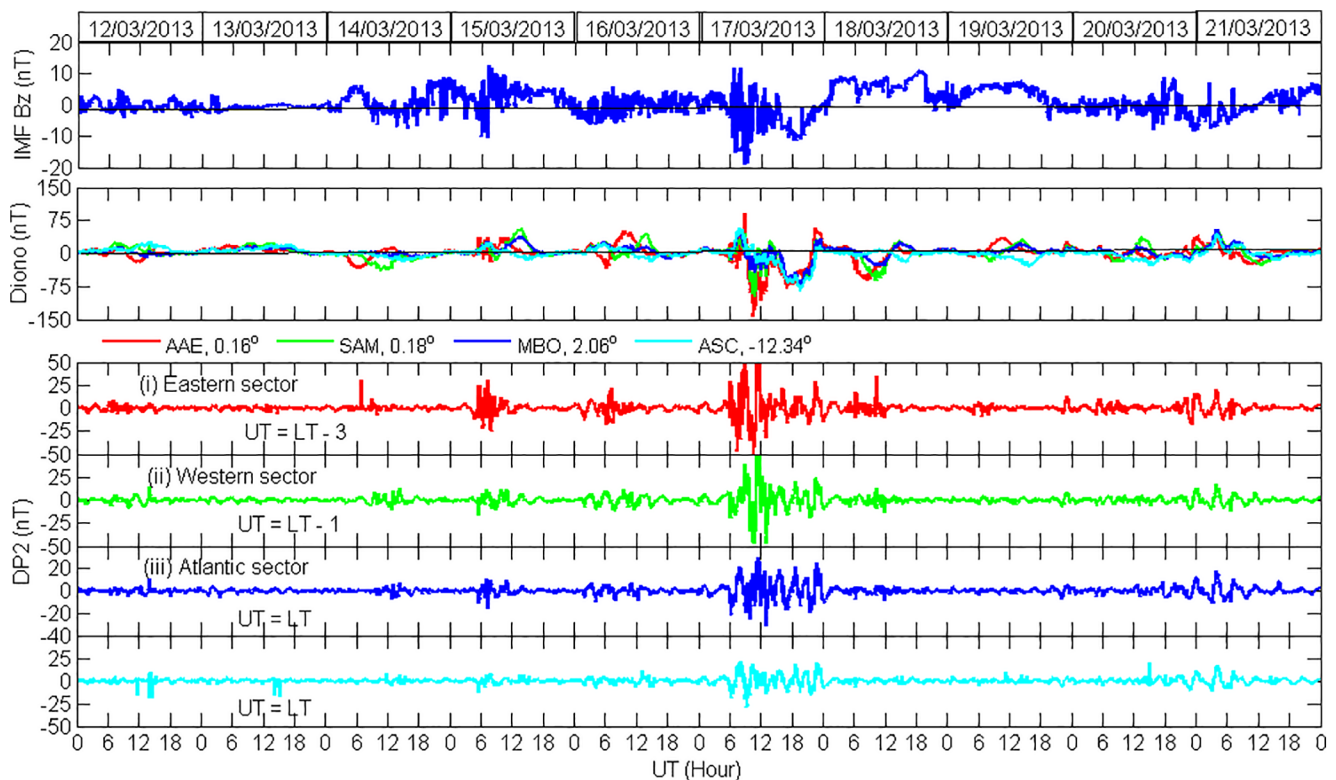
Figure 3. Variations of IMF Bz along with Diono and DP2 over Addis Ababa (red) in the Eastern sector, Samogossoni (green) in the Western sector, Mbour (blue), and Ascension Island (cyan) in the Atlantic sector from 12 to 21 March 2013.
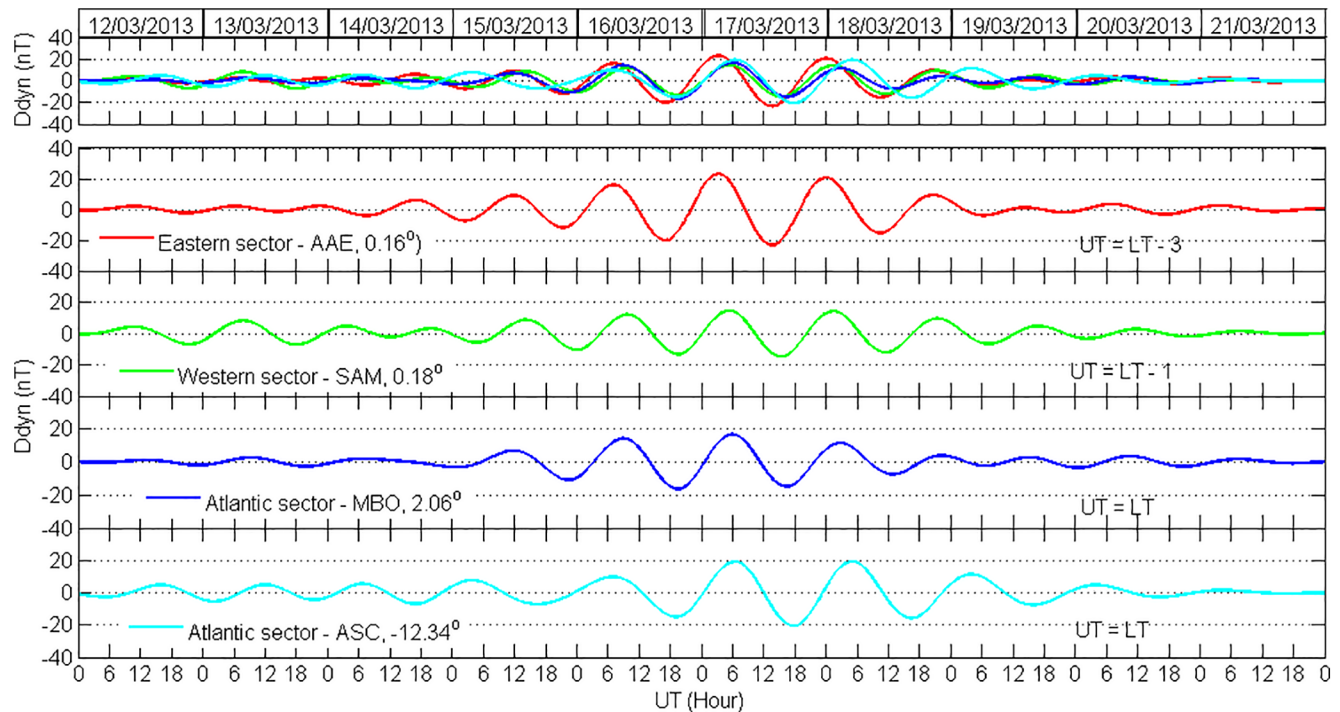
Figure 4. Variations of Ddyn over Addis Ababa (red) in the Eastern sector, Samogossoni (green) in the Western sector, Mbour (blue), and Ascension Island (cyan) in the Atlantic sector from 12 to 21 March 2013.

3.2. Variation of Ionospheric Currents

Figure 3 presents temporal variations of IMF Bz along with Diono and DP2 signals from 12 to 21 March 2013 over Addis Ababa (AAE, 9.03°N, 38.77°E, 0.16°) which is in the Eastern sector, Samogossoni (SAM, 11.60°N, 5.77°W, 0.18°) in the Western sector, Mbour (MBO, 14.39°N, 19.96°W, 2.06°) and Ascension Island (ASC, 7.95°S, 14.38°W, −12.34°) both in the Atlantic sector. From this Figure, the oscillations in Diono which occurred during the periods of southward IMF Bz corresponded well with the fluctuations of DP2 over the three sectors on 15–17 March and 20–21 March. These fluctuations were nonetheless, conspicuous on 17 March.

Figure 4 on the other hand gives an insight into the variations of Ddyn from 12 to 21 March. The diurnal Ddyn signal for the three sectors was isolated from Diono with the aid of a band pass filter. The presence of Ddyn can be seen from 15 to 19 March, but with larger (reduced) amplitude on 17 March (18 March) over all longitudinal sectors. The apparent temporal delay in Ddyn over the eastern sector was related to the difference in local time. The largest amplitude was registered in the Eastern sector while the diurnal period lasted till 19 March over the Atlantic sector.

3.3. Latitudinal Extent of Irregularities and Changes in the Postsunset Anomaly

Figure 5a presents the latitudinal extent of irregularities along longitude 25°–35°E with latitudinal extent of 40°S–40°N. We note the rather patchy nature of irregularities with weaker (stronger) amplitude at the trough (crests) as well as their extreme day-to-day variability before and after the maim phase. Generally, before the perturbation of 15 March, the latitudinal extent of irregularities spanned 8°S–27°N with intense/ strong ones (ROTI ≥ 1 TECU) occurring within 13°–23°N and 3°–8°S. On 15 March and thereafter, it reduced considerably while strong irregularities were absent from 18 to 19 March. A detailed variation in latitudinal extent of irregularities can be found in Table 2.

Figure 5b deals with variations of the postsunset anomaly from 12–21 March. The EIA was reconstructed using hourly averages of VTEC within 20:00–22:00 Local time (LT). We utilized all stations in the Eastern
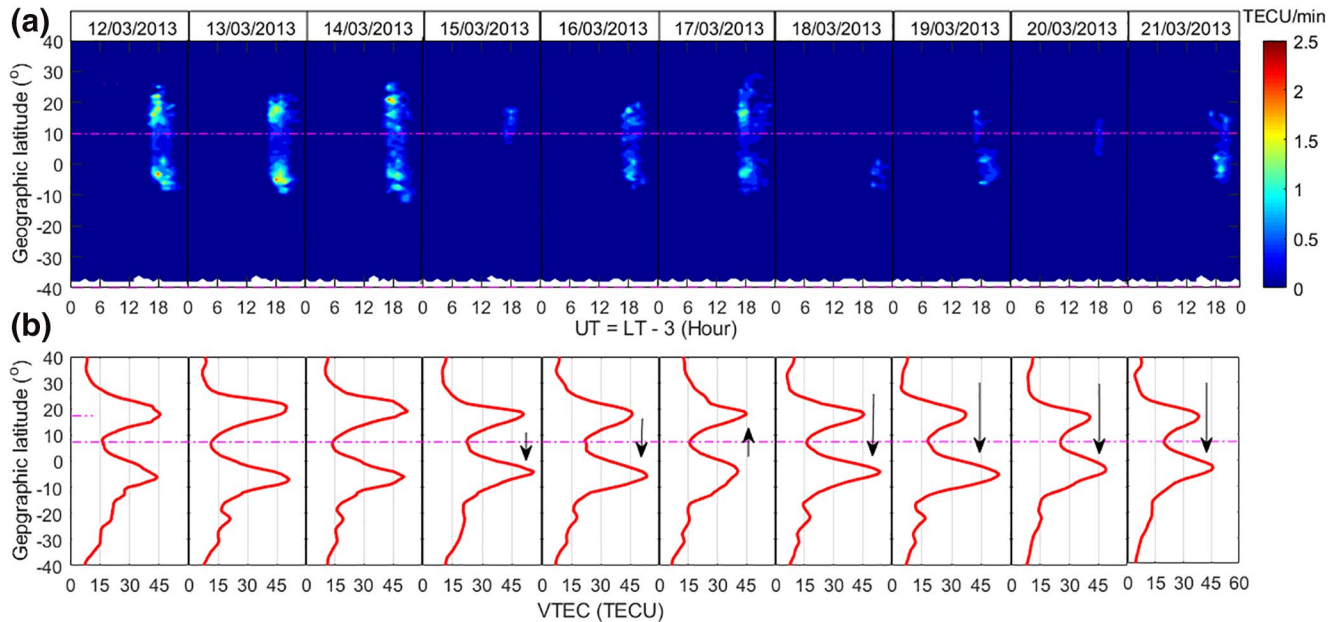
Figure 5. Latitudinal range of irregularities along longitude 25°–35°E (first panel) and latitudinal extent of the postsunset anomaly (second panel) from 12 to 21 March 2013.

longitude (Table 1 and Figure 1) within a latitudinal coverage similar to that of the ROTI maps. From Figure 5b, it can be seen that before 15 March the anomaly was relatively symmetric with the strongest crests' magnitude and highest crest-to-trough ratio (CTR). However, the level of symmetry reduced with stronger southern (northern) crest from 15 to 16 March (17 March). The EIA became conspicuously asymmetric from 18–21 March with a reduction in CTR. The Magnitude and position of the crests along with the CTR are shown in Table 2.

3.4. Postsunset Variations of C/NOFS Ni and Vz

Figure 6 displays the C/NOFS Ni and Vz variations as a function of geographic longitude and LT in the postsunset from 12 to 16 March. The satellite passed over longitude 15°W–45°E four times. However, a reasonable coverage of our longitude of interest with available data (taking into account the data selection criteria imposed in section 2) was obtained during the third orbit (third panel). Generally, the occurrence of depletions in Ni was consistent with enhancement in Vz. (See the magenta boxes in Figure 6 for some examples of depletions). The low level of ionization on 12–13 March during orbits 26687 and 26702 with coverage of 34°–45° E did not help in clearly visualizing the variations of Ni and Vz. However, a zoomed portion of the plots (not shown) revealed the presence of depletions from 20.80 to 20.91 h (on 12 March) and 20.21– to 20.35 h (on 13 March). Conspicuous depletions were nevertheless, observed from 20.45 to 21.14 h (on 13 March along 7.48°W), 20.18 to 20.57 h (14 March, 37.32°E), 20.27 to 20.68 h (15 March, 16.94°E), and 20.35 to 20.62 h (16 March, 16.61°E). The values of the enhanced Vz, their time of occurrence and longitude as well as corresponding orbit are shown in Table 2. Furthermore, we also observed a good correspondence between fluctuations in Vz and depletions in the Ni profile even when the drift was downward (negative Vz). This feature was striking during upward excursion of the drift (even though it still remained negative). Few examples are shown in the cyan boxed of Figure 6.

Figure 7 is similar to Figure 6 but is from 17–21 March. On 17 March which was the storm's main phase, the peak in Vz occurred at 19.65 h along 30.11°E during orbit 26762. This was in addition to the long duration depletion (EPB) observed from 19.90 to 20.63 h along 11.75°E during orbit 26763. Over longitude 20°–25°E, several depletions were induced during the satellite's orbit 26763. The enhancement in Vz to 82.33 ms^{-1} at 20.33 h over longitude 9.67°W was surprisingly not associated with strong depletions in Ni. Interestingly, another long depletion was observed from 21.78 to 22.43 h along 16.51°E (orbit 26764, see brown box) while

Table 2
Variations of the PRE, the Crests of the EIA and the Latitudinal Range of Irregularities From 12 to 21 March 2013

Parameter	12/03/13	13/03/13	14/03/13	15/03/13	16/03/13	17/03/13	18/03/13	19/03/13	20/03/13	21/03/13
					PRE (ms⁻¹)					
Peak Vz	23.22	39.33	37.75	58.44	13.37	39.36	13.04	29.84		
(m/s)		59.50		55.39	24.50	42.36	30.00		-	-
						82.33				
Local time (hr)	20.87	20.26	20.32	20.52	19.38	19.65	20.12	20.08		
		20.68		20.92	19.92	20.06	01.93		-	-
						20.35				
Longitude	43.47°E	35.63°E	37.32°E	16.94°E	25.52°E	30.11°E	13.37°E	13.63°E		
(degree)		7.48°W		20.92°E	8.95° E	11.75°E	19.80°E		-	-
						9.67°W				
Orbit	26687	26702	26721	26733	26747	26762	26778	26797		
		26704		26734	26748	26763	26766		-	-
						26764				
				Crest Magnitude (TECU)/Crest position (degree)						
Northern Crest	45.66/18	50.01/21	52.44/19	50.89/18	46.28/18	45.14/18	45.79/18	37.30/18	40.72/17	38.42/17
Trough	16.20/8	11.39/6	13.60/7	22.57/7	21.87/8	15.65/7	16.01/7	18.12/8	25.38/7	19.53/7
Southern Crest	44.14/−6	51.40/−7	50.68/−6	56.02/−4	53.76/−6	40.59/−4	54.13/−4	53.89/−5	48.85/−3	45.91/−3
				Crest to Trough Ration (CTR)						
CTR North	2.82	4.39	3.85	2.25	2.11	2.88	2.86	2.06	1.60	1.97
CTR South	2.72	4.51	3.73	2.48	2.45	2.59	3.38	2.97	1.92	2.35
				Latitudinal range of irregularities						
Range	8°S–26°N	9°S–23°N	13°S–27°N	8°N–19°N	8°S–20°N	9°S–31°N	8°S–2°N	7°S–19°N	2°N–15°N	7°S–18°N
				Latitudinal range of strong irregularities (ROTI≥1)						
N Hemisphere	13°–23°N	14°–20°N	15°–23°N	-	14°–18°N	14°–19°N	-	-	15°–2°N	14°–16°N
S Hemisphere	1°S–8°S	2°S–7°S	3°S–7°S	-	1°N–4°S	0°–4°S	-	-	-	2°N–3°S

the drift was upward with a peak value of 18.26 ms⁻¹ at 22.07 LT. During the recovery phase, the drift was slightly enhanced at 20.12 h (13.04 ms⁻¹) and 20.08 h (29.84 ms⁻¹) over 13.37°E and 13.63°E on 18 and 19 March, respectively (orbits 26778, 26797). Thereafter, the drift was essentially negative with several fluctuations even as several short duration depletions were still present in Ni.

3.5. Postmidnight Variations of C/NOFS Ni and Vz

Figure 8 presents a typical example of postmidnight variations in Ni and Vz as a function of longitude and local time during of 13 March (quiet day), 17 March (storm main phase) and 18 March (first day into recovery). On 13 March, there was a gradual decrease in the depletions activity from 24.00 to 3.30 h as the satellite flew from the Atlantic to the eastern sector. On 17 March, the depletions were deeper and stronger in the eastern sector than on 13 March while on 18 March they were noticeably frequent and stronger over the eastern sector. There was a corresponding gradual increase in the drift values from negative to positive until a peak of about 30 ms⁻¹ was reached at 1.93 h (19.80°E) and 2.10 h (24.40°E) on 13 and 17 March, respectively. Nevertheless, on 18 March there was a rather sharp enhancement in the drift (in contrast to its gradual increase on 13 and 17 March) to 29.90 ms⁻¹ along 0.61°W at about 0.32 h (Orbit 26766). Moreover, during orbit 26780 there was a perfect agreement between the positive enhanced drift and the occurrence of depletions over the Eastern sector. We also noted the agreement between positive enhanced drift and the occurrence of depletions on 17 March (Orbit 26752).
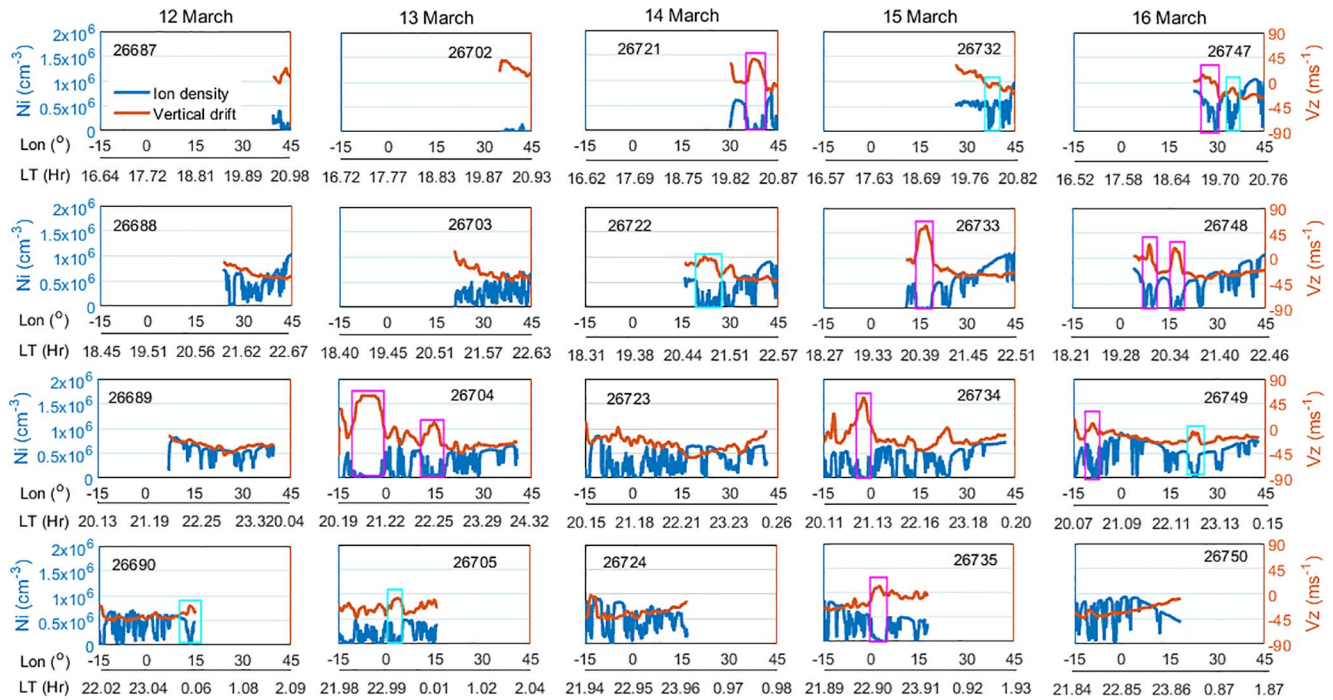
Figure 6. Ion density (blue) and vertical drift (brown) profiles as a function of geographic longitude and LT in the postsunset hours from 12 to 16 March 2013.

3.6. Longitudinal Variations of Irregularities

Figure 9 shows the longitudinal variations of irregularities quantified by the 5-min average values of ROTI over (a) the trough and (b) the crests of the anomaly from 12 to 21 March 2013. The first panel deals with stations at the trough slightly above the magnetic equator in the three sectors. The second (third) panel presents data for stations in the Western and Eastern longitudes but below the magnetic equator (at the crest of
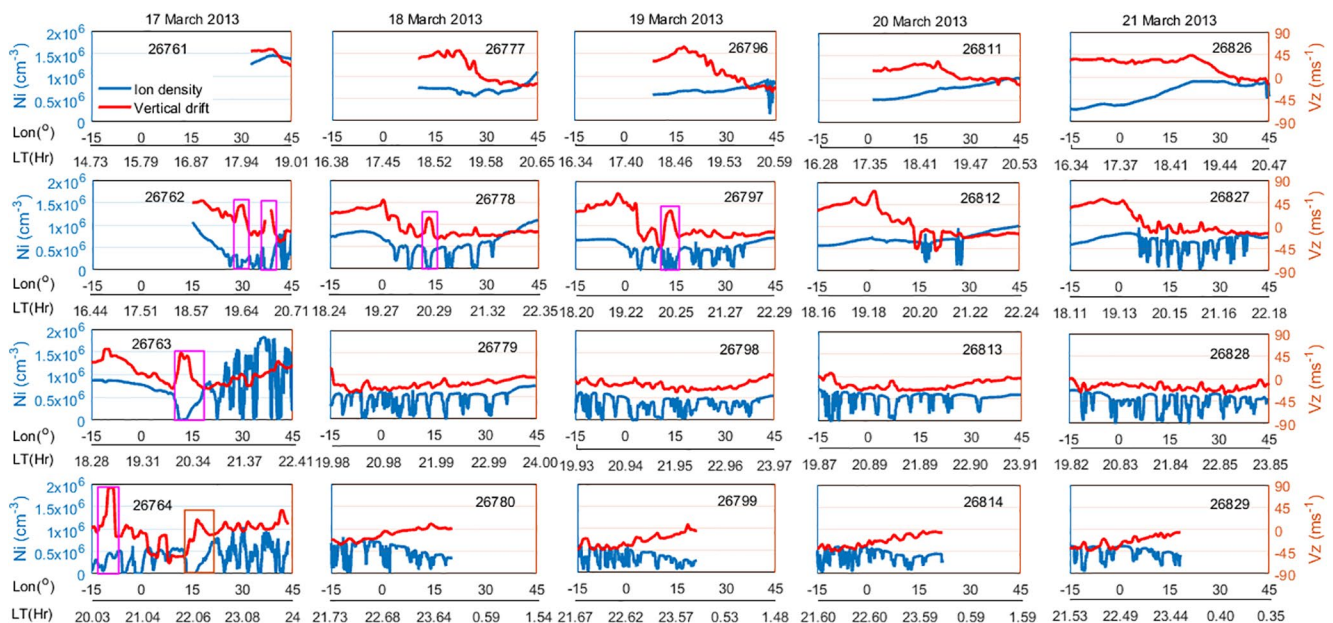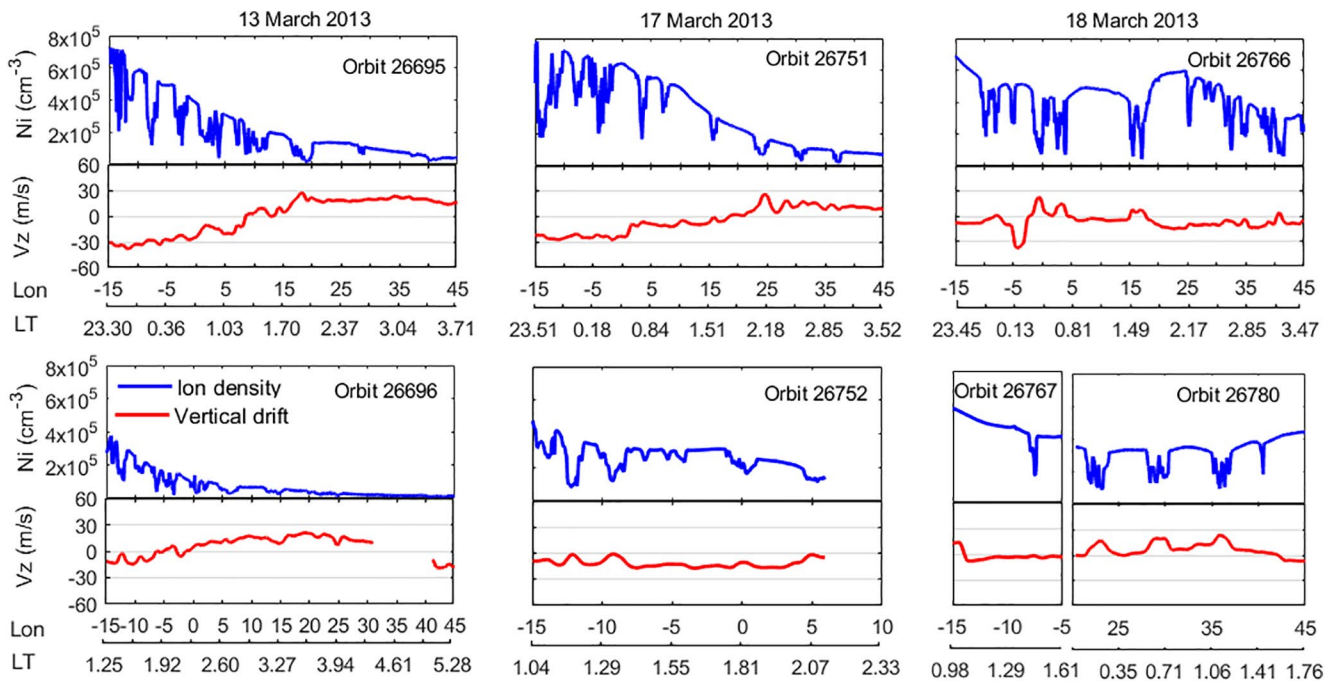

Figure 7. Ion density (blue) and vertical drift (red) profiles as a function of geographic longitude and LT in the postsunset hour from 17 to 21 March 2013.

Figure 8. Example of postmidnight variations in Ni and Vz as a function of longitude, universal and local time during of 13 March (quiet day), 17 March (storm main phase), and 18 March (first day into recovery).

the anomaly). Generally, before the main phase, the station located in the Atlantic sector (dakr , UT = LT) experienced the strongest irregularities. The strength of irregularities reduced from the station in the Western sector (cggn, UT = LT – 1) to the one in the Eastern longitude (bdmt, UT = LT – 3). On 15 March when the weak magnetic perturbation occurred, irregularities could still be seen over all stations. However, their strength was slightly reduced (when compared with the level before this day) especially, over the Eastern sector (bdmt). During the main phase, irregularities were reduced (present) over the Atlantic and Western (Eastern) sectors. During the recovery phase, from 18 to 20 March, the irregularities were strongest at the Atlantic sector, followed by the Western then Eastern sectors. Interestingly, on 21 March they were slightly
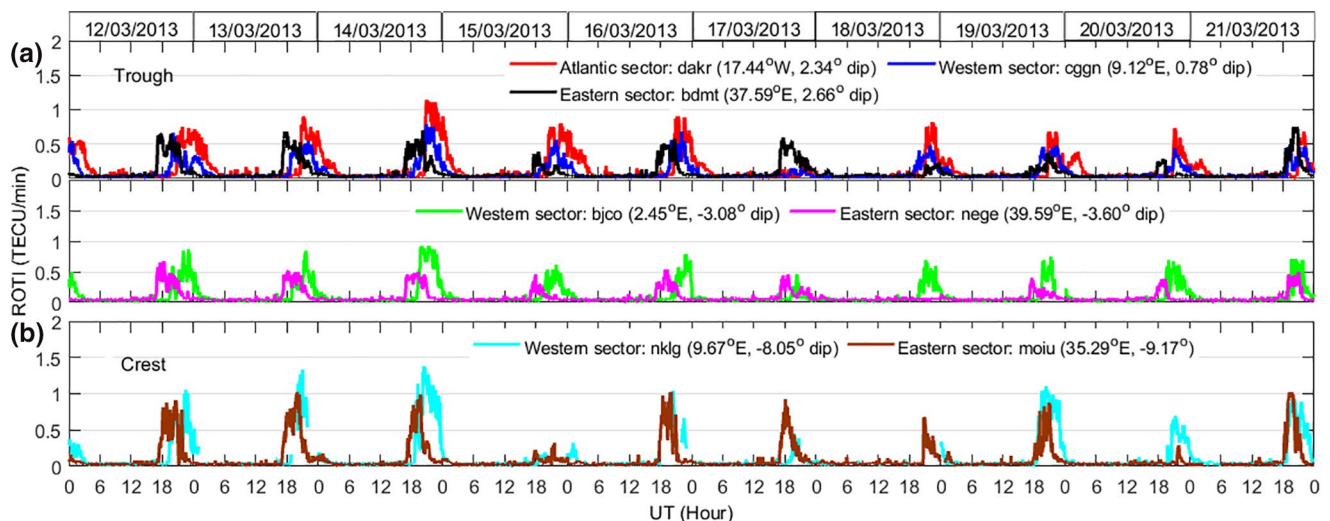
Figure 9. Longitudinal variations of irregularities over (a) the trough and (b) the crest of the EIA for the Atlantic, western and eastern sectors from 12 to 21 March 2013.

higher over the Eastern sector. From panel 3, irregularities were stronger at the anomaly crest in the Western sector (nklg, −8.05°) than the one in the Eastern sector (moiu, −9.17°) from 12 to 14 March and 19 to 20 March. On 15 March, they were clearly reduced over the Eastern station whereas the analysis at the Western station could not be performed due to data gap. On 17 March, stronger (weaker) irregularities occurred at the crest station in the Eastern (Western) sector while on 18 March there was no data for the station in the Western sector.

4. Discussion

In this section, we discussed variations of irregularities in line with mechanisms influencing their development mainly the drift, the EIA morphology, PPEF and DDEF. Thereafter, postmidnight irregularities (PMI) were examined along with longitudinal features of irregularities over Africa. Finally, a comparison with the St. Patrick storm of 2015 is made to understand the driving mechanisms during the seasonally concurrent events.

4.1. Pre-storm Vertical Plasma Drift

It has long been suggested that the PRE is a crucial parameter dictating the formation of ionospheric irregularities (Farley et al., 1970; Sultan, 1996). This is because it controls the lifting of the F-layer to altitude where the R-T instability growth rate becomes large enough to generate irregularities (B. J. Fejer et al., 1999). The storm under consideration occurred during equinox which is known for stronger drift velocities with the consequent protuberant ionospheric irregularities in the Africa longitude (Burke et al., 2004; Yizengaw et al., 2014). The drift velocities recorded on board C/NOFS were enhanced from 20.26 to 20.86 LT with peak values within 23.22–59.50 ms^{-1} before the perturbation of 15 March (Table 2 and Figure 6). This time window was clearly in line with the time of occurrence of the PRE proposed by Burke et al. (2004) and Zakharenkova et al. (2019) for Africa. It also corresponded with the time when EPBs were observed by C/NOFS (see magenta boxes in Figure 6), as well as when TEC irregularities captured by increased ROTI values were detected in the postsunset using ground-based GNSS (Figure 5a). The magnitude of the drift velocities on these days suggested an uplift of the F-layer and justified the presence of irregularities. C. S. Huang et al. (2012) had associated the presence of deep plasma bubbles with the upward drift which existed in the local time range of 19:00–21:00 LT. Previous studies have also related the onset of ESF with the development of the PRE (S. Basu et al., 1996; B. J. Fejer et al., 1999; Huang, 2018; C. S. Huang & Hairston, 2015). The drift velocities obtained in this work are well above the threshold value of ∼ 17 m/s proposed by Abdu et al. (1983) for the occurrence of spread F using the ionosonde in Fortaleza, Brazil. They are nevertheless, in line with the PRE value of about 20 m/s given by S. Basu et al. (1996) as a necessary condition for the generation of ESF on incoherent scatter radar at Jicamarca, Peru. Using measurements from the Jicamarca radar, B. J. Fejer et al. (1999) found that strong ionospheric irregularities occur when the PRE peak reaches 10 m/s near solar minimum and 50 m/s near solar maximum.

4.2. The Postsunset EIA

We observed the resurgence of a well-formed postsunset anomaly in the Eastern sector during all days with a striking change in morphology before and after the main phase (Figure 5b). If the resurgence of the EIA was driven by the PRE (Walker et al., 1994), the sudden change in its morphology could only have been induced by the geomagnetic disturbance. It has been shown that the shape of the anomaly is related to the occurrence of irregularities especially during equinox (Valladares et al., 2001). This is because the same upward drift responsible for the postsunset EIA revival also drives the formation of irregularities. From 12 to 14 March, we found a correspondence between the latitudinal extent of strong irregularities which was within 1°–8°S and 13°N–23°N (i.e., 10.45°–18.04°S and 4.03°–14.85°N dip latitude) and the latitudinal position of the anomaly crests ∼ 3°–7°S and 17–21°N (i.e., 12.52°–16.94°S and 8.24°–12.61°N dip latitude) (Table 2, row 2). We further observed a more symmetric anomaly (Figure 5b) with the highest CTR (Table 2, row 3). Higher CTR and symmetric electron density with respect to the magnetic equator in the postsunset have been found to promote irregularities activity (Maruyama & Matuura, 1984; Raghava Rao et al., 1988;

Valladares et al., 2001). We therefore, infer that in addition to PRE, stronger CTR and symmetric anomaly must have favored the development of irregularities and influenced their latitudinal extent before the storm. It is important to note that the CTR values obtained in this work are higher than the threshold of 1.4 proposed by Seba et al. (2018) for the occurrence of TEC irregularities over East Africa.

On 15–16 March, we observed an asymmetric with reduced CTR. We also noted a significant reduction in the irregularities strength and spatial extent along with stronger (weaker) drift which occurred later (earlier) on 15 March (16 March). There was nevertheless, no significant difference in the strength and shape of the anomaly on both days. This implied that the wind (not the drift) must have modulated the behavior of irregularities. The asymmetry of the anomaly with a fast decaying northern crest might be an indication of a pronounced transequatorial meridional wind. Several researchers have utilized the asymmetry of the EIA crests to infer the presence of wind (Balan et al., 1995; Khadka et al., 2018; Oyedokun et al., 2020; Valladares et al., 2001). The wind must have been generated during the auroral heating on 15 and 16 March (Figure 2, panel 4). The PC indices who are indicator of Joule heating (Troshichev et al., 2000) had higher amplitude on 15 March. Thus, stronger wind could have contributed in shaping the significant reduction in irregularities on 15 March. Maruyama and Matuura (1984) had shown that the presence of transequatorial wind has destabilizing effect on the R-T growth rate. Mendillo et al. (1992) had submitted that irregularities can be absent (reduced) even on night with rising F-layer provided that factors susceptible to inhibit them (strong meridional wind in this case) are present.

The behavior of irregularities from 19 to 21 March was similarly controlled by the morphology of the EIA and related asymmetry. The presence of westward IEFy (Figure 2, panel 3) and smallest CTR could have further supported the reduced spatial extent of irregularities on 20 March. Contrastingly, on 21 March, the formation of irregularities might have been promoted by the northward return of IMF Bz in the night (Figure 2, panel 2). The few studies on the relation between the anomaly and irregularities over Africa had focused on seasonal trends of variations in the strength of the anomaly and latitudinal extent of the crests (Amaechi et al., 2020b) as well as the values of CTR (Seba et al., 2018) during quiet time. These studies mainly revealed the asymmetry of the anomaly in winter and summer. The present work focused on the day-to-day variability of the anomaly driven by stormtime wind in equinox and its significance on irregularities occurrences in Africa. It is nonetheless, worthy to recognize the contribution of DDEF in shaping the behavior of irregularities during and after the magnetic disturbance.

4.3. Westward DDEF

PPEF and DDEF are crucial mechanisms to reckon with during geomagnetic storm as far as the occurrence of irregularities is concerned over the equatorial ionosphere. We shall start to discuss DDEF given that it first influenced irregularities during this event. The diurnal period of Ddyn from 15 to 18 March (Figure 4) was evidence of the presence of the current system related to DDEF (Blanc & Richmond, 1980; Le Huy & Amory-Mazaudier, 2005; Nava et al., 2016). Furthermore, there was a long duration westward IEFy on 18 and 19 March. These westward stormtime electric fields are known to drive downward drift hence, oppose the development of irregularities (B. G. Fejer & Scherliess, 1995). This was in line with the essentially negative drift obtained over the Eastern sector (Figure 7, red line) and the corresponding reduction in EPB activity as well as the strength and latitudinal extent of TEC irregularities (on 15–16 March). On 18 March, however, there was a complete inhibition of postsunset TEC irregularities (Figure 5a). This was due to the presence of the long lasting/strong westward DDEF (Figure 4) in conjunction with the asymmetric anomaly (Figure 5b). Evidence of the inhibition of post sunset irregularities by westward electric field has been presented in past studies (Abdu et al., 2019; Azzouzi et al., 2015; Nayak et al., 2016).

4.4. Eastward PPEF

It is known that eastward PPEF which penetrates into the low latitude can superimpose with the ambient PRE thus, causing much larger vertical drift in the postsunset (Abdu, 2019; B. G. Fejer et al., 2008). On 17 March, IMF Bz went south from about 15:30 UT (18:30 LT) with minimum value of −9.81 nT at 18:45 UT (21:45 LT in the Eastern sector). The short-term oscillations in DP2 (Figure 3) during this southward IMF Bz

condition had period lesser than 3 h and were therefore, related to eastward PPEF (Nava et al., 2016; Nishida et al., 1966). The PRE value of 39.36 ms^{-1} obtained over the Eastern sector suggested that the eastward PPEF did not significantly enhance the $\mathbf{E} \times \mathbf{B}$ drift. This could have been due to the presence of westward DDEF which was generated earlier. The superposition of both storm time electric fields nevertheless, had resulted in an upward drift which lifted the F- layer to altitude where irregularities were generated. Several EPBs were induced over the eastern sector (Figure 7, blue line) while the latitudinal range of TEC irregularities was extended to 31°N. Our result is in agreement with reports from past studies on the development and/ or intensification of EBPs due to eastward PPEF during the main phase of storms (S. Basu et al., 2007; C. Y. Huang et al., 2002; Zakharenkova et al., 2019). The observations are also in line with the results of Dugassa et al. (2019) who observed that irregularities were present on March 17, 2013 over Mbarara and Malindi, two stations located in the Eastern African sector. It is worth mentioning that TEC irregularities were less intense on this day compare to the quiet reference day. This was likely due to the smaller background ionization in the postsunset period on 17 March (Figure 5). Several researchers have stressed on the role of background ionization and its relation to irregularities formation (Aarons et al., 1981; Amaechi et al., 2020b; Tulasi Ram et al., 2006; Wernik et al., 1983). A contributing factor could have been the morphology of the EIA discussed in the past section.

4.5. Postmidnight Irregularities (PMI)

Over Africa, PMI occur essentially in June solstice (A. O. Akala et al., 2015; Amaechi et al., 2020b; Yizengaw et al., 2013). The PMI observed during this event were mainly a continuation of the postsunset activity. Irregularities after midnight were further supported by the reversal of the drift from negative to positive. On 18 March however, there was an interesting case of PMI with the resurgence of TEC irregularities over 2°N–11°S and stronger depletions in Ni especially, over the eastern sector. This was related to the long duration eastward DDEF as seen in the diurnal period of Ddyn in addition to the sharp enhancement in the upward drift to 22.30 ms^{-1} at 0.32 h over longitude 0.61°W (during orbit 26766) and the several reversals of the drift from negative to positive which occurred during orbit 26767 over the eastern sector (Figure 8). We have already stressed on the role of vertical drift and its modulating effect on the F-layer hence, on the generation of irregularities. Sahai et al. (1994) presented evidence of the generation of PMI associated with a pronounced uplift of the F-layer and the occurrence of range-type spread-F on ionosonde in the Brazilian sector during the storm of 25–26 August 1987. Past researchers have submitted that the generation of PMI is associated with magnetic activity (Kelley et al., 2003; Yizengaw et al., 2013).

4.6. Longitudinal Differences in Irregularities

Generally, TEC irregularities (Figure 9) and EPBs (Figure 6) were stronger over the Atlantic, then Western and Eastern sector during quiet days. The vertical plasma drift also followed the same longitudinal pattern before the storm's main phase. We can thus, infer that the drift was responsible for the longitudinal variation of irregularities before the storm. Zakharenkova et al. (2019) equally found that intense EPBs occurred in the Atlantic/Western than Eastern part of Africa. Our results are in line with those of Paznukhov et al. (2012) who found that the highest scintillations and EPBs occurred over the Atlantic sector during quiet period of year 2010. They suggested that changes in the PRE were responsible for this longitudinal difference. On the other hand, Mungufeni et al. (2016) submitted that the strength of irregularities reduced from west toward east and was plausibly related to the decrease in the geomagnetic field strength from east toward west over Africa.

During the main phase, the peak drift values of 82.33 ms^{-1}, 39.36 ms^{-1}, and 42.36 ms^{-1} were recorded over the Atlantic (9.67°W), Western (11.75°E) and Eastern (30.11°E) sector, respectively. The enhancement in the drift was as a result of the eastward PPEF. Surprisingly, the enhanced drift corresponded only to weak EPBs and reduced TEC irregularities over Dakar (17.44°W) which is the Atlantic sector. Oppositely, the PPEF induced a long duration EPBs along 11.75°E in the Western sector. This corresponded with weak TEC irregularities in Toro (9.12°E) and Libreville (9.67°E) both in the Western sector. Also, more depletions in Ni occurred over the Eastern sector during the main phase. The presence of irregularities over the Eastern sector has already been discussed. We suggest that their reduction over the Atlantic and Eastern sectors might

have been related to stormtime equatorial neutral wind. We had also discussed the effects of the presence of the wind and its suppressive effect on irregularities irrespective of the positive drift. The longitudinal difference in irregularities on 17 March might have thus, been modulated by the difference in stormtime wind over Africa. There was no wind data or sufficient GNSS receivers to reconstruct the postsunset EIA and infer the presence of the wind from its shape over the entire longitude of interest. Abe et al. (2018) had suggested that the asymmetry in irregularities over the Western and Eastern sector during the equinoctial month of October 2013 was driven by transequatorial meridional wind. Dugassa et al. (2019) observed a triggering (inhibition) of irregularities over the Eastern (Western) sector on March 17, 2017. Previous studies have mainly suggested that the longitudinal difference in irregularities over Africa was driven by the time of occurrence of PPEF/DDEF (Amaechi et al., 2018a; Azzouzi et al., 2015; Dugassa et al., 2019; Ngwira et al., 2013). In this study, we have stressed on the contribution of stormtime wind in driving these differences during the main phase of this storm.

On the other hand, postsunset irregularities were present (absent) over the Atlantic/Western (Eastern) sector on 18 March. We have already shown that their absence over the Eastern sector was due to long duration DDEF. Nonetheless, their presence over the Atlantic/Western sector can only be explained in terms of weak DDEF that failed to suppress the PRE. From Figure 4, the diurnal period of Ddyn first decayed over the Atlantic, and was relatively weaker over the Western sector. We further observed positive drift although with reduced strength over the Atlantic/Western sector.

4.7. Comparison with the St. Patrick Storm of March 17, 2015

Comparing the St. Patrick's Day Geomagnetic Storm of March 2013 with that of 2015 will offer us an insight into various mechanisms responsible for irregularities variations during disturbed conditions in Africa. A striking coincidence between both events is the day of occurrence (day of the year, DOY, 76) while an obvious difference is their occurrence during various phases of solar cycle 24; the first (second) during the maximum (descending) phase. From the study of Amaechi et al. (2020a), the level of irregularities before and after the main phase appeared to be stronger during the March 2015 than March 2013 event. This could be understood in terms of the higher solar flux of 126.89 and 111.36 sfu registered in March 2015 and March 2013, respectively. Higher solar flux is often associated with stronger drift thus, higher irregularities.

From the solar and interplanetary perspective, both events were associated Halo Coronal Mass Ejections (CMEs) on 15 March, with higher space speed during the first (1366 km/s) than second (932 km/s) event (Scolini et al., 2018). We note that Halo CMEs are much faster and more energetic as such will have more impact in the magnetosphere. The related ICME resulted in a shock and difference in the interplanetary structure that determined the nature of the ionospheric response in term of irregularities variations. For example, during the first event, auroral activity parametized by the Auroral Activity (AE) index was intense and started immediately after the shock (06:00 UT) while during the second, there was no preloading of energy into the magnetotail and as such no substorm (Verkhoglyadova et al., 2016). Also, the ring current and the time of occurrence and duration of the southward IMF Bz played an important role in driving the electrodynamics. The storm of 2013 was characterized by a double southward IMF Bz occurring in the sheath (with SYM-H minimum of −107 nT at 10:28 UT and 11:55 UT) and another southward turning in the magnetic cloud (MC) (SYM-H ~ −132 nT at 20:52 UT). That of 2015 was also marked by a southward turning of IMF Bz within the sheath (SYM-H ~ -101 nT at 09:36 UT) but a northward turning resulting in a quick recovery phase. Furthermore, there were two others southward IMF Bz turnings including a long duration one (SYM-H ~ −150 nT at 17:28 UT, SYM-H ~ −234 nT at 22:47 UT) in the MC, with the continuation of auroral activity and a prolonged recovery phase due to the High-speed stream on DOY 77 (Verkhoglyadova et al., 2016).

As for the ionospheric response, the intensification of TEC irregularities and occurrence of strong EPBs during the main phase of the storm of March 17, 2013 was in contrast with their complete inhibition on March 17, 2015. Using C/NOFS data, Zakharenkova et al. (2019) showed that EPBs were completely suppressed on March 17, 2015 over the African longitude. Carter et al. (2014) also observed the inhibition of scintillations associated with a reduction in the R-T instability growth rate over Africa while Amaechi et al. (2018b) found that TEC irregularities were absent on the same day. The difference between both events

was mainly driven by the strength of PPEF and DDEF. On March 17, 2013 (March 17, 2015) eastward PPEF (westward DDEF) occurred in the postsunset period and enhanced (suppressed) irregularities. Another significant difference between both events was the duration of DDEF. During the storm of March 17, 2013, the diurnal Ddyn period was observed before March 17, 2013 and lasted just 1–2 days into the recovery phase. Oppositely, for the March 17, 2015 event, it lasted 6 days starting from the main phase (Nava et al., 2016) and had a reduced amplitude from 20 to 22 March over the Eastern sector (Amaechi et al., 2020a). The difference in the duration of DDEF during both events was related to the pre-existing disturbance before the main phase of the earlier storm (March 17, 2013) and the strength/duration of auroral heating during the latter one (March 17, 2015).

One important similarity between both events is perhaps the complete inhibition of postsunset TEC irregularities on 18 March. It has been shown that TEC irregularities (Amaechi et al., 2018b; Bolaji et al., 2019; Zakharenkova et al., 2019) and scintillation index (S4) (Carter et al., 2016) were inhibited over Africa on March 18, 2015. Also, postmidnight EPBs were triggered during both storms. Moreover, we found that the strongest EPB occurred mostly over the Atlantic and Western sector before the storm of March 2013. Same observation was made by Zakharenkova et al. (2019) during quiet condition in March 2015. A new result from the present study is the intensification of EPBs activity in the postsunset sector (postmidnight) on 17 March (18 March) 2013 over the Eastern sector only. Surprisingly, no postmidnight TEC irregularities were observed using ground-based GNSS on March 18, 2015 (Amaechi et al., 2018b; Bolaji et al., 2019).

5. Conclusion

Variations of ionospheric irregularities have been examined in Africa during the St. Patrick storm of March 17, 2013. We have exploited GNSS ROTI, magnetometer data and C/NOFS in-situ ion density and vertical drift measurements over longitude 15°W–45°E from 12 to 21 March 2013. The important findings from results are as follows:

(i) The observed signature of PRE with vertical drift velocity from 23.22 to 59.50 ms^{-1} during 20.26–20.86 LT corresponds to the occurrence of postsunset EPBs and TEC irregularities. The strength of irregularities apparently increased from the Atlantic, then Western and Eastern longitude in line with variations of the PRE.

(ii) Over the Eastern sector, the latitudinal extent of postsunset irregularities which spanned 8.00°–27.00°N (18.04°S–19.46°N dip latitude) before the storm was extended to 31.00°N (24.17° dip latitude) in the northern hemisphere during the main phase.

(iii) The latitudinal variation of the position of the postsunset crests (3°–7°S and 17–21°N) fell well within the latitudinal distribution of strong TEC irregularities (1°–8°S and 13°N–23°N) over the Eastern sector before the storm.

(iv) During the main phase, the combined eastward PPEF and westward DDEF resulted in an upward drift that induced several depletions over the Eastern sector in addition to a long duration EPBs along 11.75°E. Over the Atlantic and Western sectors however, the enhanced PRE corresponded only to weak depletion/irregularities. This longitudinal difference could have been related to stormtime wind.

(v) On 18 March, postsunset/postmidnight irregularities were inhibited/triggered by the long duration westward/eastward DDEF over the Eastern sector only. Several depletions in the C/NOFS ion density were also observed over this sector mostly in the postmidnight.

(vi) There was a significant change in the morphology of the EIA which was more asymmetric with reduced CTR during the recovery phase. This also corresponded to the reduction in the latitudinal extent of irregularities to 2.00°N–15.00°N (7.28°S–6.12°N dip latitude).

Over the years, GNSS has played a substantial role in enhancing the operational efficiency of critical systems used for precise positioning, navigation and timing. However, ionospheric irregularities which are an important component of space weather adversely impact on the performance of GNSS. The outcomes of our analysis thus, underpin the characteristic ionospheric delay error, loss of lock probability and TEC gradients at the EIA region which pose a serious challenge to GNSS users in Africa especially, during space weather. These include aircraft and maritime navigation in the adjacent areas of the Atlantic and Indian Oceans as

well as mobile phone networks that use GNSS timing for network synchronization over the continent. The findings from the study therefore provides users of these applications with useful information on the sporadic nature and intensity of irregularities as well as their spatial and temporal extent, mostly at the vicinity of the magnetic equator (±25° dip) in the postsunset to postmidnight, along with the eventual disruption and reduction in the operational capability of their applications in Africa.

Mitigating space weather effect on critical technologies however, requires continuous investigations with multi-instrument data sets across the African longitude. Such investigations are fundamental to the reliable deployment of ionospheric delay error forecasting and mitigation services. This include the Satellite Based Augmentation Systems (SBAS) and the European Geostationary Navigation Overlay Service (EGNOS) introduced to facilitate higher cadence aviation and maritime navigation as well as cellular services which more than before rely on GNSS in and around the African region.

Data Availability Statement

GNSS data used in this study were provided by the UNAVCO Facility (hfps://www.unavco.org) with support from the National Science Foundation (NSF) and National Aeronautics and Space Administration (NASA). The WAMNET magnetometer network is funded by the Center National d'Etudes Spatiales (CNES), and is maintained by the Institut de Physique du Globe de Paris (IPGP). Data are made available through bcmt. fr/wamnetwork.html.

References

Aarons, J., Mullen, J. P., Whitney, H. E., Johnson, A. L., & Weber, E. J. (1981). UHF scintillation activity over polar latitudes. *Geophysical Research Letters*, *8*(3), 277–280. https://doi.org/10.1029/GL008i003p00277

Abdu, M. A., 2019. Day-to-day and short-term variabilities in the equatorial plasma bubble/spread F irregularity seeding and development. *Progress in Earth and Planetary Science*, *6*, 11. https://doi.org/10.1186/s40645-019-0258-1

Abdu, M. A., de Medeiros, R. T., Bittencourt, J. A., & Batista, I. S. (1983). Vertical ionization drift velocities and range type spread F in the evening equatorial ionosphere. *Journal of Geophysical Research*, *88*(A1), 399–402. https://doi.org/10.1029/JA088iA01p00399

Abe, O. E., Rabiu, A. B., & Radicella, S. M. (2018). Longitudinal asymmetry of the occurrence of the plasma irregularities over African low-latitude region. *Pure and Applied Geophysics*, *175*(12), 4355–4370.

Akala, A. O., Amaeshi, L. L. N., Somoye, E. O., Idolor, R. O., Okoro, E., Doherty, P. H., et al. (2015). Climatology of GPS amplitude scintillations over equatorial Africa during the minimum and ascending phases of solar cycle 24. *Astrophysics and Space Science*, *357*(17), 1–9. https://doi.org/10.1007/s10509-015-2292-9

Akala, A. O., Awoyele, A., & Doherty, P. H. (2016). Statistics of GNSS amplitude scintillation occurrences over Dakar, Senegal, at varying elevation angles during the maximum phase of solar cycle 24. *Space Weather*, *14*, 233–246. https://doi.org/10.1002/2015SW001261

Akala, A. O., Ejalonibu, A. H., Doherty, P. H., Radicella, S. M., Groves, K. M., Carrano, C. S., et al. (2017). Characterization of GNSS amplitude scintillations over Addis Ababa during 2009–2013. *Advances in Space Research*, *59*, 1969–1983.

Akala, A. O., Oyeyemi, E. O., Amaechi, P. O., Radicella, S. M., Nava, B., & Amory-Mazaudier, C. (2020). Longitudinal responses of the equatorial/low-latitude ionosphere over the oceanic regions to geomagnetic storms of May and September 2017. *Journal of Geophysical Research: Space Physics*, *125*, e2020JA027963. https://doi.org/10.1029/2020JA027963

Amaechi, P. O., Oyeyemi, E. O., & Akala, A. O. (2018a). The response of African equatorial/low-latitude ionosphere to 2015 St. Patrick's Day geomagnetic storm. *Space Weather*, *16*, 601–618. https://doi.org/10.1029/2017SW001751

Amaechi, P. O., Oyeyemi, E. O., & Akala, A. O. (2018b). Geomagnetic storm effects on the occurrences of ionospheric irregularities over the African equatorial/low-latitude region. *Advances in Space Research*, *61*, 2070–2090.

Amaechi, P. O., Oyeyemi, E. O., Akala, A. O., & Amory-Mazaudier, C. (2020a). Geomagnetic activity control of irregularities occurrences over the crests of the African EIA. *Earth and Space Science*, *7*(7), e2020EA001183.

Amaechi, P. O., Oyeyemi, E. O., Akala, A. O., Falayi, E. O., Kaab, M., Benkhaldoun, Z., et al. (2020b). Quiet time ionoperic irregularities over the African equatorial ionization anomaly (EIA) region. *Radio Science*, *55*(8), e2020RS007077. https://doi.org/10.1029/2020RS007077

Azzouzi, I., Migoya-Orue, Y., Amory-Mazaudier, C., Fleury, R., Radicella, S. M., & Touzani, A. (2015). Signature of solar event at middle and low latitudes in the European-African sector, during geomagnetic storms. *Advances in Space Research*, *56*(9), 2040–2055. https://doi.org/10.1016/j.asr.2015.06.010

Balan, N., Bailey, J. J., Moffett, R. J., Su, Y. Z., & Titheridge, J. E. (1995). Modeling studies of the conjugate-hemisphere differences in ionospheric ionization at equatorial anomaly latitudes. *Journal of Atmospheric and Terrestrial Physics*, *57*(3), 279–292.

Basu, S., Basu, S., Makela, J. J., Sheehan, R. E., Makenzie, E., Doherty, P., et al. (2005). Two components of ionospheric plasma structuring at middle latitudes observed during the magnetic storm of October 30, 2003. *Geophysical Research Letters*, *32*, L12S06. https://doi.org/10.1029/2004GL021669

Basu, S., Basu, S., Rich, F. J., Groves, K. M., MacKenzie, E., Coker, C. (2007). Response of the equatorial ionosphere at dusk to penetration electric fields during intense magnetic storms. *Journal of Geophysical Research*, *112*(8), A08308. https://doi.org/10.1029/2006JA012192

Basu, S., Kudeki, E., Basu, S., Valladares, C. E., Weber, E. J., Zengingonul, H. P., et al. (1996). Scintillations, plasma drifts, and neutral winds in the equatorial ionosphere after sunset. *Journal of Geophysical Research*, *101*(A12), 26795–26809. https://doi.org/10.1029/96JA00760

Berkner, L. V., & Wells, H. W. (1934). F-region ionosphere investigation at low altitudes. *Terrestrial Magnetism and Atmospheric Electricity*, *39*, 215.

Bhattacharyya, A., Fedrizzi, M., Fuller-Rowell, T. J., Gurram, P., Kakad, B., Sripathi, S., et al. (2019). Effect of magnetic storm related thermospheric changes on the evolution of equatorial plasma bubbles. *Journal of Geophysical Research*, *124*(3), 2256–2270 https://doi.org/10.1029/2018JA025995

Blanc, M., & Richmond, A. D. (1980). The ionospheric disturbance dynamo. *Journal of Geophysical Research*, *85*, 1669–1686. https://doi.org/10.1029/JA085iA04p01669

Bolaji, O. S., Adebiyi, S. J., & Fashae, J. B. (2019). Characterization of ionospheric irregularities at different longitudes during quiet and disturbed geomagnetic conditions. *Journal of Atmospheric and Solar-Terrestrial Physics*, *182*, 93–100.

Buonsanto, M. J. (1999). Ionspheric storms-a review. *Space Science Reviews*, *88*, 563–601.

Burke, W. J., Gentile, L. C., Huang, C. Y., Valladares, C. E., & Su, S. Y. (2004). Longitudinal variability of equatorial plasma bubbles observed by DMSP and ROCSAT- 1. *Journal of Geophysical Research*, *109*, A12301. https://doi.10.1029/2004JA010583

Carter, B. A., Yizengaw, E., Retterer, J. M., Francis, M., Terkildsen, M., Marshall, R., et al. (2014). An analysis of the quiet time day-to-day variability in the formation of postsunset equatorial plasma bubbles in the Southeast Asian region. *Journal of Geophysical Research*, *119*, 3206–3223. https://doi.org/10.1002/2013JA019570

Carter, B. A., Yizengaw, E., Pradipta, R., Retterer, J. M., Groves, K., & Valladares, C. (2016). Global equatorial plasma bubble occurrence during the 2015 St. Patrick's Day storm. *Journal of Geophysical Research: Space Physics*, *121*(1), 894–905.

Chakrabarty, D., Sekar, R., Narayanan, R., Devasia, C. V., & Pathan, B. M. (2005). Evidence for the interplanetary electric field effect on the OI 630.0 nm airglow over low latitude. *Journal of Geophysical Research*, *110*, A11301. https://doi.org/10.1029/2005JA011221

Cherniak, I., Krankowski, A., & Zakharenkova, I., 2018. ROTI maps: A new IGS ionospheric product characterizing the ionospheric irregularities occurrence. *GPS Solutions*, *22*, 69. https://doi.org/10.1007/s10291-018-0730-1

de Abreu, A. J., Martin, I. M., Fagundes, P. R., Venkatesh, K., Batista, I. S., de Jesus, R., et al. (2017). Ionospheric F-region observations over American sector during an intense space weather event using multi-instruments. *Journal of Atmospheric and Solar-Terrestrial Physics*, *156*, 1–14. http://dx.doi.org/10.1016/j.jastp.2017.02.009

de La Beaujardière, O., & the C/NOFS Science Definition Team (2004). C/NOFS: A mission to forecast scintillations. *Journal of Atmospheric and Solar-Terrestrial Physics*, *66*(17), 1573–1591. https://doi.org/10.1016/j.jastp.2004.07.030

Dugassa, T., Habarulema, J. B., & Nigussie, M. (2019). Longitudinal variability of occurrence of ionospheric irregularities over the American, African and Indian regions during geomagnetic storms. *Advances in Space Research*, *63*(2019), 2609–2622.

Dungey, J. W. (1956). Convective diffusion in the equatorial F region. *Journal of Atmospheric and Terrestrial Physics*, *9*(5–6), 304–310.

Estey, L. H., & Meertens, C. M. (1999). TEQC: The multi-purpose toolkit for GPS/GLONASS data. *GPS Solutions*, *3*(1), 42–49. https://doi.org/10.1007/PL00012778

Farley, D. T., Balsey, B. B., Woodman, R. F., & McClure, J. P. (1970). Equatorial spread F: Implications of VHF radar observations. *Journal of Geophysical Research*, *75*(34), 7199–7216. https://doi.org/10.1029/JA075i034p07199

Fejer, B. G., Jensen, J. W., & Su, S. Y. (2008). Quiet time equatorial F region vertical plasma drift model derived from ROCSAT-1 observations. *Journal of Geophysical Research*, *113*, A05304. https://doi.org/10.1029/2007JA012801

Fejer, B. G., & Scherliess, L. (1995). Time dependent response of equatorial ionoapheric electric fields to magnetospheric disturbances. *Geophysical Research Letters*, *22*, 851. https://doi.org/10.1029/95GL00390

Fejer, B. J., Scherliess, L., & de Paula, E. R. (1999). Effects of the vertical plasma drift velocity on the generation and evolution of equatorial spread F. *Journal of Geophysical Research: Space Physics*, *104*(A9), 19859–19869.

Gonzalez, W. D., Joselyn, J. A., Kamide, Y., Kroehl, H. W., Rostoker, G., Tsurutani, B. T., et al. (1994). What is a geomagnetic storm?. *Journal of Geophysical Research 99*(A4), 5771–5792. https://doi.org/10.1029/93JA02867

Gonzalez, W. D., Tsurutani, B. T., & De Gonzalez, A. L. C. (1999). Interplanetary origin of geomagnetic storms. *Space Science Reviews*, *88*(3–4), 529–562.

Huang, C. S. (2011). Occurrence of equatorial plasma bubbles during intense magnetic storms. *International Journal of Geophysics*, *2011*, 401858. https://doi.org/10.1155/2011/401858

Huang, C.-S. (2018). Effects of the post sunset vertical plasma drift on the generation of equatorial spread F. *Progress in Earth and Planetary Science*, *5*, 3. https://doi.org/10.1186/s40645-017-0155-4

Huang, C. Y., Burke, W. J., Machuzak, J. S., Gentile, L. C., & Sultan, P. J. (2001). DMSP observations of equatorial plasma bubbles in the topside ionosphere near solar maximum. *Journal of Geophysical Research*, *106*(A5), 8131–8142. https://doi.org/10.1029/2000JA000319

Huang, C. Y., Burke, W. J., Machuzak, J. S., Gentile, L. C., & Sultan, P. J. (2002). Equatorial plasma bubbles observed by DMSP satellites during a full solar cycle: Toward a global climatology. *Journal of Geophysical Research*, *107*(12), 1434. https://doi.org/10.1029/2002JA009452

Huang, C. S., de La Beaujardiere, O., Roddy, P. A., Hunton, D. E., Ballenthin, J. O., & Hairston, M. R. (2012). Generation and characteristics of equatorial plasma bubbles detected by the C/NOFS satellite near the sunset terminator. *Journal of Geophysical Research*, *117*, A11313. https://doi.org/10.1029/2012JA018163

Huang, C.-S., & Hairston, M. R. (2015). The postsunset vertical plasma drift and its effects on the generation of equatorial plasma bubbles observed by the C/NOFS satellite. *Journal of Geophysical Research: Space Physics*, *120*, 2263–2275. https://doi.org/10.1002/2014JA020735

Hudson, M. K., & Kennel, C. F. (1975). Linear theory of equatorial spread F. *Journal of Geophysical Research*, *80*(34), 4581–4590. https://doi.org/10.1029/JA080i034p04581

Iyemori, T., & Rao, D. R. K. (1996). Decay of the Dst field of geomagnetic disturbance after substorm onset and its implication to storm-substorm relation. *Annales Geophysicae*, *14*, 608–618.

Kelley, M. C., Haldoupis, C., Nicolls, M. J., Makela, J. J., Belehaki, A., Shalimov, S., et al. (2003). Case studies of coupling between the E and F regions during unstable sporadic-E conditions. *Journal of Geophysical Research: Space Physics*, *108*, 1447. https://doi.org/10.1029/2003JA009955

Khadka, S. M., Valladares, C. E., Sheehan, R., & Gerrard, A. J. (2018). Effects of electric field and neutral wind on the asymmetry of equatorial ionization anomaly. *Radio Science*, *53*(5), 683–697.

Le Huy, M., & Amory-Mazaudier, C. (2005). Magnetic signature of the ionospheric disturbance dynamo at equatorial latitudes: "Ddyn". *Journal of Geophysical Research*, *110*, A10301. https://doi.org/10.1029/2004JA010578

Luo, X., Xiong, C., Gu, S., Lou, Y., Stolle, C., Wan, X., et al. (2019). Geomagnetically conjugate observations of equatorial plasma irregularities from Swarm constellation and ground-based GPS stations. *Journal of Geophysical Research: Space Physics*, *124*(5), 3650–3665. https://doi.org/10.1029/2019JA026515

Luo, W., Zhu, Z., Xiong, C., & Chang, S. (2017). The response of equatorial ionization anomaly in 120° E to the geomagnetic storm of 18 August 2003 at different altitudes from multiple satellite observations. *Space Weather*, *15*(12), 1588–1601.

Maruyama, T., Ma, G., & Tsugawa, T. (2013). Storm-induced plasma stream in the low-latitude to midlatitude ionosphere. *Journal of Geophysical Research: Space Physics*, *118*(9), 5931–5941. https://doi.org/10.1002/jgra.50541

Maruyama, T., & Matuura, N. (1984). Longitudinal variability of annual changes in activity of equatorial spread F and plasma bubbles. *Journal of Geophysical Research*, *39*, 10903–10912. https://doi.org/10.1029/JA089iA12p10903

Mendillo, M., Baumgardner, J., Pi, X., & Sultan, P. J. (1992). Onset conditions for equatorial spread F. *Journal of Geophysical Research*, *97*(A9), 13865–13876. https://doi.org/10.1029/92JA00647

Mungufeni, P., Habarulema, J. B., & Jurua, E. (2016). Trends of ionospheric irregularities over African low latitude region during quiet geomagnetic conditions. *Journal of Atmospheric and Solar Terrestrial Physics*, *138*, 261–267.

Nava, B., Rodríguez-Zuluaga, J., Alazo-Cuartas, K., Kashcheyev, A., Migoya-Orué, Y., Radicella, S. M., et al. (2016). Middle and low latitude ionosphere response to 2015 St. Patrick's Day geomagnetic storm. *Journal of Geophysical Research: Space Physics*, *121*, 3421–3438. https://doi.org/10.1002/2015JA022299

Nayak, C., Tsai, L. -C., Su, S. -Y., Galkin, I., Caton, R., & Groves, K. (2016). Suppression of ionospheric scintillation during St. Patrick's 24 Day geomagnetic super storm as observed over the anomaly crest region station Pingtung, Taiwan: A case study. *Advances in Space Research*, *60*, 396–405.

Ngwira, C. M., Seemala, G. K., & Habarulema, J. B. (2013). Simultaneous observations of ionospheric irregularities in the African low-latitude region. *Journal of Atmospheric and Solar-Terrestrial Physics*, *97*, 50–57.

Nishida, A. (1968). Geomagnetic DP2 fluctuations and associated magnetospheric phenomena. *Journal of Geophysical Research*, *73*, 173. https://doi.org/10.1029/JA073i005p01795

Nishida, A., Iwasaki, T., & Nagata, T. (1966). The origin of fluctuations in the equatorial electrojet: A new type of geomagnetic variation. *Annales de Geophysique*, *22*, 478–484.

Oyedokun, O. J., Akala, A. O., & Oyeyemi, E. O. (2020). Characterization of African equatorial ionization anomaly (EIA) during the maximum phase of solar cycle 24. *Journal of Geophysical Research: Space Physics*, *125*(9), e2019JA027066. https://doi.org/10.1029/2019ja027066

Paznukhov, V., Carrano, C., Doherty, P. H., Caton, R., Valladares, C. E., Groves, K. M., et al. (2012). Equatorial plasma bubbles and L-band scintillations in Africa during solar minimum. *Annales Geophysicae*, *30*, 675–682.

Perkins, F. W. (1975). Ionospheric irregularities. *Reviews of Geophysics and Space Physics*, *3*(13), 884.

Pi, X., Mannucci, A. J., Lindqwister, U. J., & Ho, C. M. (1997). Monitoring of global ionospheric irregularities using the worldwide GPS network. *Geophysical Research Letters*, *24*(18), 2283–2286.

Raghava Rao, R., Nageswararao, M., Sastri, J. H., Vyas, G. D., & Sriramarao, M. (1988). Role of equatorial ionization anomaly in the initiation of equatorial spread F. *Journal of Geophysical Research: Space Physics*, *93*(A6), 5959–5964. https://doi.org/10.1029/JA093iA06p05959

Rama Rao, P. V. S., Niranjan, K., Prasad, D. S. V. V. D., Gopi, S. K., & Uma, G. (2006). On the validity of the ionospheric pierce point (IPP) altitude of 350 km in the Indian equatorial and low-latitude sector. *Annales Geophysicae*, *24*, 2159–2168.

Rodrigues, F. S., Crowley, G., Azeem, S. M. I., & Heelis, R. A. (2011). C/NOFS observations of the equatorial ionospheric electric field response to the 2009 major sudden stratospheric warming event. *Journal of Geophysical Research*, *116*, A09316. https://doi.org/10.1029/2011JA016660

Sahai, Y., Aarons, J., Mendillo, M., Baumgardner, J., Bittencourt, J. A., & Takahashi, H. (1994). OI 630 nm imaging observations of equatorial plasma depletions at 16 S dip latitude. *Journal of Atmospheric and Terrestrial Physics*, *56*(11), 1461–1475.

Sardón, E., & Zarraoa, N. (1997). Estimation of total electron content using GPS data: How stable are the differential satellite and receiver instrumental biases?. *Radio Science*, *32*(5), 1899–1910.

Scolini, C., Messerotti, M., Poedts, S., & Rodriguez, L., 2018. Halo coronal mass ejections during solar cycle 24: Reconstruction of the global scenario and geoeffectiveness. *Journal of Space Weather Space Climate*, *8*, A09.

Seba, E. B., Nigussie, M., & Moldwin, M. B. (2018). The relationship between equatorial ionization anomaly and nighttime equatorial spread F in East Africa. *Advances in Space Research*, *62*(7), 1737–1752.

Seemala, G., & Delay, S. B. (2010). *GNSS TEC data processing2nd workshop on satellite navigation science and technology for Africa*. Trieste: 6–24 April 2010.

Seemala, G., & Valladares, C. (2011). Statistics of total electron content depletions observed over the South American continent for the year 2008. *Radio Science*, *46*, RS5019. https://doi.org/10.1029/2011RS004722

Shreedevi, P. R., & Choudhary, R. K. (2017). Impact of oscillating IMF Bz during 17 March 2013 storm on the distribution of plasma over Indian low-latitude and mid-latitude ionospheric regions. *Journal of Geophysical Research: Space Physics*, *122*, 11607–11623. https://doi.org/10.1002/2017JA023980

Stolle, C., Lühr, H., Rother, M., & Balasis, G. (2006). Magnetic signatures of equatorial spread F as observed by the CHAMP satellite. *Journal of Geophysical Research*, *111*, A02304. https://doi.org/10.1029/2005JA011184

Su, S. Y., Liu, C. H., Ho, H. H., & Chao, C. K. (2006). Distribution characteristics of topside ionospheric density irregularities: Equatorial versus midlatitude regions. *Journal of Geophysical Research*, *111*, A06305. https://doi.org/10.1029/2005JA011330

Sultan, P. J. (1996). Linear theory and modeling of the Rayleigh-Taylor instability leading to the occurrence of equatorial spread F. *Journal of Geophysical Research*, *101*(A12), 26875–26891. https://doi.org/10.1029/96JA00682

Sulungu, E. D., & Uiso, C. (2019). Ionospheric TEC response to geomagnetic storms occurred on 15-20 March 2013 and 2015 over the eastern Africa region. *American Journal of Environmental Science and Engineering*, *3*(4), 103–111.

Troshichev, O. A., Lukianova, R. Y., Papitashvili, V. O., Rich, F. J., & Rasmussen, O. (2000). Polar cap index (PC) as a proxy for ionospheric electric field in the near-pole region. *Geophysical Research Letters*, *27*(23), 3809–3812. https://doi.org/10.1029/2000GL003756

Tulasi Ram, S., Rao, P. R., Niranjan, K., Prasad, D. S. V. V. D., Sridharan, R., Devasia, C. V., & Ravindran, S. (2006). The role of post-sunset vertical drifts at the equator in predicting the onset of VHF scintillations during high and low sunspot activity years. *Annales Geophysicae*, *24*(6), 1609–1616.

Valladares, C. E., Basu, S., Groves, K., Hagan, M. P., Hysell, D., Mazzella, A. J., Jr, et al. (2001). Measurement of the latitudinal distributions of total electron content during equatorial spread F events. *Journal of Geophysical Research: Space Physics*, *106*(A12), 29133–29152. https://doi.org/10.1029/2000JA000426

Valladares, C. E., Villalobos, J., Hei, M. A., Sheehan, R., Basu, S., MacKenzie, E., et al. (2009). Simultaneous observation of traveling ionospheric disturbances in the Northern and Southern Hemispheres. *Annales de Geophysique*, *27*, 1501–1508.

Verkhoglyadova, O. P., Tsurutani, B. T., Mannucci, A. J., Mlynczak, M. G., Hunt, L. A., Paxton, L. J., et al. (2016). Solar wind driving of ionosphere-thermosphere responses in three storms near St. Patrick's Day in 2012, 2013, and 2015. *Journal of Geophysical Research: Space Physics*, *121*(9), 8900–8923. https://doi.org/10.1002/2016JA022883

Walker, G. O., Ma, J. H. K., & Gotton, E. (1994). The equatorial ionosphere anomaly in electron content for solar maximum to solar minimum to solar maximum at South East Asia. *Annales Geophysicae*, *12*, 195–209.

Wernik, A. W., Liu, C. H., & Yeh, K. C. (1983). Modeling of spaced-receiver scintillation measurements. *Radio Science*, *18*(05), 743–764.

Whalen, J. A. (2002). Dependence of equatorial bubbles and bottomside spread F on season, magnetic activity, and E×B drift velocity during solar maximum. *Journal of Geophysical Research*, *107*(A2), SIA–3. https://doi.org/10.1029/2001JA000039

Woodman, R. F. (1970). Vertical drift velocities and east-west electric fields at the magnetic equator. *Journal of Geophysical Research*, *75*, 6249–6259. https://doi.org/10.1029/JA075i031p06249

Woodman, R. F., & La Hoz, C. (1976). Radar observations of F region equatorial irregularities. *Journal of Geophysical Research*, *81*(31), 5447–5466. https://doi.org/10.1029/JA081i031p05447

Xu, L., Cheng, G., Xu, J., & Liu, Y. (2008). Global ionospheric TEC response to a strong magnetic storm. *Science in China - Series E: Technological Sciences*, *51*(10), 1786–1802.

Xu, Z., Hartinger, M. D., Clauer, C. R., Peek, T., & Behlke, R. (2017). A comparison of the ground magnetic responses during the 2013 and 2015 St. Patrick's Day geomagnetic storms. *Journal of Geophysical Research: Space Physics*, *122*, 4023–4036. https://doi.org/10.1002/2016JA023338

Yizengaw, E., & Groves, K. M. (2018). Longitudinal and seasonal variability of equatorial ionospheric irregularities and electrodynamics. *Space Weather*, *16*(8), 946–968.

Yizengaw, E., Moldwin, M. B., Zesta, E., Biouele, C. M., Damtie, B., Mebrahtu, A., et al. (2014). The longitudinal variability of equatorial electrojet and vertical drift velocity in the African and American sectors. *Annales Geophysicae*, *32*(3), 231–238.

Yizengaw, E., Retterer, J., Pacheco, E. E., Roddy, P., Groves, K., Caton, R., et al. (2013). Postmidnight bubbles and scintillations in the quiet-time June solstice. *Geophysical Research Letters*, *40*(21), 5592–5597. https://doi.org/10.1002/2013GL058307

Yue, X., WangLei, W. J., Burns, A., Zhang, Y., Wan, W., Liu, L., et al. (2016). Long-lasting negative ionospheric storm effects in low and middle latitudes during the recovery phase of the 17 March 2013 geomagnetic storm. *Journal of Geophysical Research: Space Physics*, *121*, 9234–9249. https://doi.org/10.1002/2016JA022984

Zakharenkova, I., Cherniak, I., & Krankowski, A. (2019). Features of storm-induced ionospheric irregularities from ground-based and spaceborne GPS observations during the 2015 St. Patrick's Day storm. *Journal of Geophysical Research: Space Physics*, *124*, 10728–10748. https://doi.org/10.1029/2019ja026782